Surface-directed dynamics in living liquid crystals

Aditya Vats,[1] Varsha Banerjee,[1] and Sanjay Puri[2]
[1]*Department of Physics, Indian Institute of Technology Delhi, New Delhi 110016, India*
[2]*School of Physical Sciences, Jawaharlal Nehru University, New Delhi 110067, India*

(Received 11 January 2024; accepted 7 August 2024; published 3 September 2024)

We study living liquid crystals (LLCs), which are an amalgam of nematic liquid crystals (LCs) and active matter (AM). These LLCs are placed in contact with surfaces which impose planar/homeotropic boundary conditions on the director field of the LC and the polarization field of the AM. The interplay of LC-AM interactions and the surface-directed conditions yield controlled pattern dynamics in the LLC, which has important technological implications. We discuss two representative examples of this pattern dynamics.

DOI: 10.1103/PhysRevE.110.034701

I. INTRODUCTION

Active matter (AM) is an important example of an inherently nonequilibrium system which exhibits coherent dynamics on a much larger scale than the constituent units. These units can be biological or synthetic, ranging from micrometers to meters, e.g., polar gels, bacterial suspensions, micro-tubule bundles, cytoplasmic streaming, bird flocks, fish shoals, vibrating granular rods, etc. [1,2]. Active particles continuously consume energy from the surroundings and convert it to motion. They hold promise for creating miniature machines. For example, a bacterial bath can generate persistent motion in tiny gears utilized as devices for harvesting energy [3–6]. Although apparently coordinated, AM can exhibit irregular behavior on larger scales as collisions with the medium particles cause random tumblings. The utility of AM can be greatly enhanced with the possibility of organized or tailored flows. For example, directed trajectories can be utilized in cargo transport or targeted drug delivery [7–9].

A contemporary system of relevance in the above context is *living liquid crystals* (LLCs), or a suspension of active particles such as bacteria in nematic liquid crystals (LCs) [10–15]. The latter, composed of rod-shaped molecules or *nematogens*, are classic examples of anisotropic fluids having long-range orientational order below a critical temperature T_c. In this nematic phase, the nematogens align along a preferred direction called the *director*, while maintaining positional fluidity [16,17]. It should be stressed that the LLCs are distinct from the much-studied *active nematics* [18,19]. The latter system consists of rod-shaped active particles that spontaneously organize in large-scale structures with orientational order and self-sustained flows. On the other hand, in LLCs, the nematic properties and the activity are characteristics of two distinct subsystems. The strong LC-AM coupling substantially alters the collective behavior of the two-component system. An important experimental fact in LLCs is the co-alignment of the active particles and the nematogens [10,12,20]. Consequently, the active particles swim parallel to the director, and topological defects in LCs play a significant role in transporting these swimmers. Experiments have reported a preferential movement of bacteria from defects with $-1/2$ charge towards defects with $+1/2$ charge [12,13]. The active particles also perturb the director field at macroscopic length scales, and reveal important information about the visco-elastic properties of the LC medium. Further, the self-propulsion energy gets stored in director perturbations that can be harnessed into useful work [21,22]. Clearly, LLCs offer many pathways for the control of one component (AM or LC) by the other (LC or AM). This opens up the possibility of diverse scientific and technological applications.

Many experiments have shown that boundary conditions imposed at container surfaces can significantly impact pattern formation and dynamics in active systems [23–32]. The surface-directed dynamics differs substantially from the bulk dynamics, and often exhibits novel features. It has been reported that boundaries can act as sources or sinks of orientational order, leading to patterns such as stripes, vortices, and clusters [26,33–36]. They are also known to self-organize and stabilize patterns that would otherwise be unstable in the bulk. In an important experiment, Peng *et al.* [11] generated a predetermined bulk configuration by appropriate surface treatment of the bounding plates in LLCs.

The effect of confinement has also been well-studied in the context of pure LCs in the square well geometry [37–44]. An interesting aspect of the square well geometry, in contrast to thin films and cylindrical geometries, is the frustration at sharp corners. Boundary anchoring in nematic-filled square wells has been exploited to control topological defects and obtain tailored morphologies. In particular, LC square wells were found to be bistable without any external field [38,39]. A natural extension is to study confinement in LCs with inclusions. In this system, we can expect rich pattern formation due to the possibility of distinct boundary conditions for the two components, and their interplay due to coupling. In an earlier work, we performed extensive numerical studies to obtain equilibrium states of LCs with magnetic inclusions or *ferronematics* confined to (i) one-dimensional channels, and (ii) two-dimensional wells [45,46]. In (i), we observed an unexpected polydomain structure in the weak coupling limit without the application of magnetic fields. However, the one-dimensional nature of the problem limits the solution landscape for both the nematic and magnetic order parameters

[45]. In (ii), exotic stable nematic and associated magnetization morphologies were observed, induced purely by the geometry, the boundary conditions, and the coupling between the magnetic nanoparticles and the host nematic medium [46].

In this paper, we perform similar investigations for LLCs which (in contrast to ferronematics) are an out-of-equilibrium system due to the perpetual activity of the inclusions. For example, can tailored structures in LC square wells be exploited for directed transport of AM? Alternatively, can tailored flows dictated by boundary conditions on AM be used to create novel configurations in LCs? Finally, and perhaps most important, can the symbiotic interplay of these components plus boundary conditions yield hitherto unknown states of AM and LCs? The dual possibility of (a) tailoring active trajectories around novel defect configurations in LCs, and (b) the erasure of topological defects in LCs by active flows offers intriguing design concepts for microfluidic devices. We will address these and related questions from a theoretical perspective in the present paper.

An earlier study on pattern formation in LLCs used circular confinement to mimic the natural geometry in the experiments [14]. In this work, we consider LLCs confined in square wells. As discussed above, this is a well-studied geometry both in experiments and theoretical studies of LCs, thereby providing useful benchmarks. We use the phenomenological kinetic model for LLCs developed in our recent work [47]. This model consists of the Toner-Tu (TT) model for AM [48,49], the time-dependent Ginzburg-Landau (TDGL) model for the LC [50,51], and an experimentally motivated coupling term which favors co-alignment of the two components. Our theoretical studies of this model in the bulk demonstrated two novel steady states: *chimeras* and *solitons*, which sweep through the coupled system in synchrony. Further, the symbiotic dynamics of the AM and LC can be exploited to induce and manipulate order in a component which is intrinsically (i.e., in the absence of coupling) disordered. Some of the natural questions to address in the context of confinement are as follows: Will the equilibrium nematic morphologies remain stable in the presence of active entities? Can we control the active particle trajectories by tailoring the topological defects in the nematic component? How do different boundary conditions affect the emergent structures from this coupling between nematic order and activity?

The rest of our paper is organized as follows. In Sec. II, we describe our coarse-grained modeling of LLCs. We also discuss typical boundary conditions which are imposed on the order parameters. In Sec. III, we present detailed numerical results from our simulations of these models. We conclude this paper with a summary and discussion in Sec. IV.

II. MODELING OF LIVING LIQUID CRYSTALS

We employ an order-parameter-based description for the LLCs. This phenomenological approach uses free energy functionals based on the symmetries of the order parameters describing the system. For the nematic component, the order parameter is the **Q**-tensor, which is a symmetric, traceless matrix whose leading eigenvector is the director **n**. The components of **Q** can be written as $Q_{ij} = \mathcal{S}(n_i n_j - \delta_{ij}/d)$, where d is the dimensionality. The scalar order parameter $\mathcal{S}$ measures the degree of orientational order about **n**. For example, $\mathcal{S} = 1$ describes a fully aligned nematic state, and a disordered state corresponds to low order with $\mathcal{S} \simeq 0$. The *Landau-de Gennes* (LdG) free energy for the LC can be written as [16,52–54]

$$F_Q[\mathbf{Q}] = \int d\mathbf{r}\left\{\frac{A}{2}\mathrm{Tr}(\boldsymbol{Q}^2) + \frac{B}{3}\mathrm{Tr}(\boldsymbol{Q}^3) + \frac{C}{4}[\mathrm{Tr}(\boldsymbol{Q}^2)]^2 + \frac{L}{2}|\nabla\mathbf{Q}|^2\right\}, \tag{1}$$

where A, B, C, and L are phenomenological parameters. We have $A = A_0(T - T_c)$, where A_0 is a material-dependent coefficient and T_c is the critical temperature for LC ordering. The gradient term in Eq. (1) penalizes local variations in the order parameter.

Although AM is inherently nonequilibrium, one can formulate the TT model via a suitable "free energy". This is defined as a functional of the two "order parameters": local density $\rho(\mathbf{r}, t)$ (which is conserved) and the polarization field $\mathbf{P}(\mathbf{r}, t)$ (which is nonconserved). The quantity $\mathbf{P}(\mathbf{r}, t)$ measures the local orientation of AM. The free energy in terms of these order parameters is given by [2]

$$F_a[\rho, \mathbf{P}] = \int d\mathbf{r}\left[\frac{\alpha(\rho)}{2}|\mathbf{P}|^2 + \frac{\beta}{4}|\mathbf{P}|^4 + \frac{\kappa}{2}|\nabla\mathbf{P}|^2 + \frac{w}{2}|\mathbf{P}|^2\nabla \cdot \mathbf{P} - \frac{v_1}{2}(\nabla\cdot\mathbf{P})\frac{\delta\rho}{\rho_0} + \frac{D_\rho}{2}(\delta\rho)^2\right], \tag{2}$$

where $\alpha, \beta, \kappa, w, v_1, D_\rho$ are material-dependent parameters whose values can be related to the microscopic properties of the active particles [55]. In Eq. (2), $\delta\rho = \rho - \rho_0$, where ρ_0 is the average density of the system. The parameter $\alpha(\rho) = \alpha_0(1 - \rho/\rho_c)$, where α_0 is a positive constant and ρ_c is the critical density. This free energy yields a continuous phase transition from a disordered state (with $\rho = \rho_0$ and $\mathbf{P} = 0$ for $\rho_0 < \rho_c$) to an ordered state (with $\rho = \rho_0$ and $|\mathbf{P}| \sim \sqrt{(\rho_0/\rho_c - 1)}$ for $\rho_0 > \rho_c$). The TT model is written in terms of F_a [2], as will be discussed shortly. For the TT model with densities just above the transition point ($\rho \gtrsim \rho_0^+$), the ordered phase is unstable, and the system relaxes to a banded state that sweeps the system with speed v_0 (which is the same as the speed of active particles).

In recent work [47], we have proposed that the "free energy" of LLCs can be written as the sum of F_Q and F_a, along with a suitable coupling term F_c: $F[\mathbf{Q}, \rho, \mathbf{P}] = F_Q[\mathbf{Q}] + F_a[\rho, \mathbf{P}] + F_c[\mathbf{Q}, \rho, \mathbf{P}]$. Experimental observations on LLCs dictate that active particles tend to align along the nematic director, i.e., $\mathbf{P} \parallel \mathbf{n}$ [10,12]. The dyadic product of the **Q**-tensor and the polarization vector **P** is the lowest order term that ensures this co-alignment and the $\mathbf{n} \to -\mathbf{n}$ symmetry. With these considerations, the free energy contribution from the coupling can be written as

$$F_c[\mathbf{Q}, \mathbf{P}] = -c_0 \sum_{i,j} Q_{ij} P_i P_j, \tag{3}$$

where c_0 is the strength of the AM-LC interaction. The coupling term is equivalent to $-c_0(\mathbf{n}\cdot\mathbf{P})^2$, which manifestly promotes co-alignment if $c_0 > 0$. The phenomenological parameter c_0 represents the anchoring strength on the surface

of active matter, and yields elastic torques which ensure that active particles swim parallel to the local director. This term is included to mimic the experimental observations in LLCs that report co-alignment of bacteria with the LC molecules [11,12,14,27]. For $c_0 < 0$, the preferred orientation is $\mathbf{P} \perp \mathbf{n}$. It is also possible to model the situation where $\mathbf{P}$ and $\mathbf{n}$ are aligned at an arbitrary angle, though the corresponding F_c is more complicated than Eq. (3).

The dissipative dynamics of LCs is studied via the TDGL equation for nonconserved kinetics [56]:

$$\frac{\partial \mathbf{Q}}{\partial t} = -\Gamma_Q \frac{\delta F_Q}{\delta \mathbf{Q}}, \tag{4}$$

where Γ_Q is the kinetic coefficient. For simplicity, we present the corresponding LLC equations in $d = 2$ here. In that case, $\mathbf{Q}$ is a 2×2 matrix:

$$\mathbf{Q} = \begin{pmatrix} Q_{11} & Q_{12} \\ Q_{12} & -Q_{11} \end{pmatrix}. \tag{5}$$

This form of the $\mathbf{Q}$-tensor respects the up-down symmetry of the nematic components, and ensures that the director remains in two dimensions [40–43]. For the nematic components in LLCs, the corresponding TDGL equations are as follows [47]:

$$\frac{\partial Q_{11}}{\partial t} = -\Gamma_{\mathbf{Q}} \frac{\delta F_Q[\mathbf{Q}]}{\delta Q_{11}} + \Gamma_{\mathbf{Q}} c_0 \left(P_1^2 - P_2^2\right), \tag{6}$$

$$\frac{\partial Q_{12}}{\partial t} = -\Gamma_{\mathbf{Q}} \frac{\delta F_Q[\mathbf{Q}]}{\delta Q_{12}} + \Gamma_{\mathbf{Q}} c_0 (2 P_1 P_2). \tag{7}$$

Here, the damping parameter Γ_Q sets the relaxation time scale for the system. The first term on the right-hand-side of Eqs. (6)–(7) relaxes the pure LC to its free energy minimum. The second term represents the correction due to the coupling with AM. The model excludes the velocity fields of the nematic components, and is appropriate in the high-density limit where hydrodynamic flows are rapidly dissipated. In such a scenario, the relaxation dynamics is primarily governed by intermolecular interactions rather than fluid flow in nematic liquid crystals. Further, the free energy formulation can be generalized to incorporate spatially anisotropic elastic constants which are experimentally relevant. At present, we do not incorporate this anisotropy. Our isotropic model already shows rich dynamics, as we show in Ref. [47] as well as in this paper. We expect much of this pattern dynamics to survive for moderate anisotropy.

The AM dynamics is governed by the TT equations for the density and polarization fields [48,49]. As mentioned earlier, the TT model for pure AM can be formulated using a "free energy" F_a [2]. The incorporation of the coupling term F_c in F_a yields the relevant $d = 2$ equations for AM in LLCs as follows [47]:

$$\frac{\partial \rho}{\partial t} = -v_0 \nabla \cdot (\mathbf{P}\rho) - \nabla \cdot \left(-\Gamma_\rho \nabla \frac{\delta F_a}{\delta \rho}\right), \tag{8}$$

$$\frac{\partial P_1}{\partial t} = \lambda_1 (\mathbf{P} \cdot \nabla) P_1 - \Gamma_{\mathbf{P}} \frac{\delta F_a}{\delta P_1} + \Gamma_{\mathbf{P}} c_0 (Q_{11} P_1 + Q_{12} P_2), \tag{9}$$

$$\frac{\partial P_2}{\partial t} = \lambda_1 (\mathbf{P} \cdot \nabla) P_2 - \Gamma_{\mathbf{P}} \frac{\delta F_a}{\delta P_2} + \Gamma_{\mathbf{P}} c_0 (Q_{12} P_1 - Q_{11} P_2). \tag{10}$$

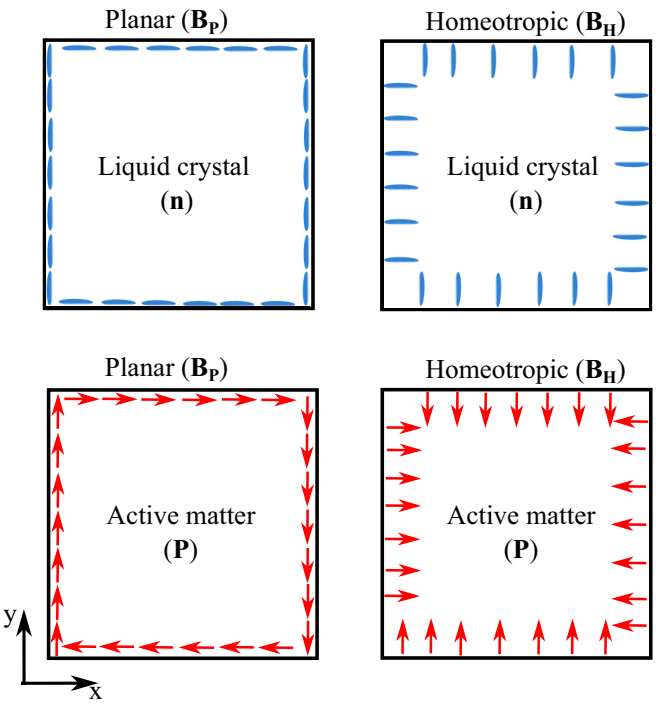

FIG. 1. Schematic depicting planar (B_P) and homeotropic (B_H) boundary conditions for nematic (upper frames) and active (lower frames) components.

Here, Γ_ρ and $\Gamma_{\mathbf{P}}$ set the relaxation time scales for the density and polarization fields. The first term on the RHS of Eqs. (9)–(10) describes the effect of advection on the flow alignment. Its prefactor λ_1 has the dimensions of speed. The terms with c_0 in Eqs. (9)–(10) model the effect of the AM-LC coupling. The dimensionless versions of Eqs. (6)–(10) are provided in Appendix. We use these coupled equations as a model for LLCs in this paper. According to the Mermin-Wagner theorem, continuous symmetries cannot be spontaneously broken in $d \leqslant 2$ at nonzero temperature in equilibrium systems with short-range interactions. Perhaps the most interesting aspect of AM is that this intrinsically nonequilibrium system does exhibit long-range order even in $d = 2$ [48,49]. Thus, the $d = 2$ results presented here may be expected to foreshadow $d = 3$ results.

In our previous work [47], we focused on symbiotic dynamics of this model in the bulk. Our focus in the present work is the opposite, viz., whether we can control the dynamics of the AM and LCs by placing them in contact with a surface which exerts specific boundary conditions. We are motivated by the possibility of regulating pattern dynamics in the context of technological applications. Some quantitative statements about the nature of boundary conditions and the corresponding solutions in pure LCs and AM are in order. In the present work, we have studied all possible combinations of planar (B_P) and homeotropic (B_H) conditions for both components (see the schematic in Fig. 1). The vector order parameter ($\mathbf{n}$ or $\mathbf{P}$) is anchored parallel (perpendicular) to the walls in planar (homeotropic) conditions. There are also additional possibilities for boundary conditions. These arise by (a) mixing B_P and B_H for $\mathbf{n}$ and $\mathbf{P}$ on different surfaces in

Fig. 1; and (b) by flipping $\mathbf{P} \to -\mathbf{P}$ on ore or more surfaces in the lower frames of Fig. 1. For simplicity, we will restrict ourselves to the conditions depicted in Fig. 1.

These conditions are well-established in the literature for LC square wells [37,39,40,45,46], and can be readily implemented in a physical setting. For example, the surface can be treated chemically to favor specific anchoring conditions on the nematic director. Other mechanisms to achieve the desired director orientation for LCs include lithography, surface anchoring, flow alignment and coupling to an external field [16,57]. In the context of AM, planar boundary conditions are most commonly used. The presence of geometric constraints is enough to implement these in experiments. For homeotropic conditions, experiments suggest that the confining walls can comprise different particles, and the potential between the active and wall particles can be tuned to achieve the desired boundaries [24]. Setting up physical barriers or optical traps, predefined surface patterning and chemical modification are other commonly used techniques employed to set boundary conditions in AM [58].

III. NUMERICAL RESULTS

A. Computational Details

We have used the Euler discretization method [59] to numerically solve Eqs. (A2)–(A6) and determine the evolution of the nematic and active components. The discretization mesh sizes used in our simulations are $\Delta x = \Delta y = 1$ and $\Delta t = 0.01$. These mesh sizes satisfy the stability criteria of the uncoupled system, i.e., the TDGL equation for the nematic, and the Toner-Tu equations for active matter. The initial fields $\mathbf{Q}(\mathbf{r}, 0)$ and $\mathbf{P}(\mathbf{r}, 0)$ consist of small random fluctuations about 0, corresponding to the disordered state. Similarly, the initial density field $\rho(\mathbf{r}, 0)$ consists of small fluctuations about ρ_0. Thus, we study coarsening of the system from a disordered state at $t = 0$. Notice that all the coupling terms in Eqs. (A2)–(A5) are quadratic. Therefore, the growth of linear fluctuations about the disordered state is the same as for the uncoupled system ($c_0 = 0$). The effect of the coupling is manifested only when the fields enter a nonlinear growth regime. The equations are solved using the different boundary conditions in Fig. 1 for $\mathbf{n}$ and $\mathbf{P}$. We use periodic boundary conditions for ρ. The parameters are such that $T < T_c$ (+ sign in Eqs. (A2)–(A3)) and $\rho = \rho_c^+ = 0.52$. In the bulk (mimicked by periodic boundary conditions for all fields), these parameters yield a uniform ordered phase for the nematic, and a banded state for the AM [47]. We have confirmed the stability of the steady states presented subsequently by trying 10 independent initial conditions, and arriving at the same states. Further, although we will show evolution snapshots for different boundary conditions at $t = 10^4$, we have verified that the system maintains the corresponding states till $t = 2 \times 10^5$.

B. Results for the Uncoupled System ($c_0 = 0$)

We start by discussing the consequences of planar and homeotropic boundary conditions for uncoupled systems, i.e., $c_0 = 0$. This will provide a reference point to judge the effect of the coupling. There have been many studies of both nematic [37,39–43,45,60] and active components [23–29,33–36,61,62] in this context. In this limit, both fields evolve independently. Figures 2(a)–2(b) show nematic morphologies at $t = 10^4$ for planar (B_P) and homeotropic (B_H) boundary conditions. The color bar indicates the magnitude of the orientational order parameter $\mathcal{S}$. A topological defect of charge $+1/2$ ($-1/2$) in the nematic medium is identified as a point around which the orientation of the (apolar) director changes by $+\pi$ ($-\pi$) when traversed clockwise. Naturally, the order parameter $\mathcal{S} \simeq 0$ at the defect. In Figs. 2(a)–2(b), the director $\mathbf{n}$ (denoted by rods) aligns diagonally in the square well indicating the absence of bulk defects for both B_P and B_H. The elastic term penalizes the variation of the director field in the bulk, whereas the strong anchoring condition is imposed only at the boundaries. Their competition leads to topological structures reminiscent of partial defects at the corners. The director field at the corners rotates by $\pi/2$. This morphology has also been observed experimentally in LCs confined in square wells with homeotropic boundary conditions [39].

The corresponding $\mathbf{P}$-field for the active component is shown in Figs. 2(c) and 2(d). The arrows represent the orientation $\mathbf{P}$. The active medium has $+1$ (-1) defects, corresponding to points where $\mathbf{P}$ rotates by 2π (-2π) when traversed clockwise. For B_P, there is a single $+1$ defect which moves around in the system. This is expected as the planar anchoring at the boundaries yields a singular vortex. Further, the advection term in the system causes the vortex to circulate within the bulk inducing the swirling active flow. Similar observations have also been made in previous studies by Sokolov *et al.* [14] in which the AM was confined to circular substrates with B_P BCs. For B_H, there are multiple defects in the system [as shown in Fig. 2(d)] with a complicated dynamical interplay. The imposition of homeotropic boundaries leads to a chaotic state characterized by the spontaneous generation and annihilation of defects throughout the system. We argue that the strong anchoring in opposite directions at adjacent boundary edges prevents the system from adopting singular defect dynamics, thus resulting in the observed chaotic state.

The Supplemental Material (SM) [63] shows movies (M1) of the evolution for Figs. 2(c)–2(d). The color bar adjacent to Figs. 2(c)–2(d) denotes the magnitude $|\mathbf{P}|$ – this goes to 0 at the defect cores. As expected, ρ in Figs. 2(e)–2(f) tracks the ρ-variation due to the ρ-$\mathbf{P}$ coupling in the TT equations. We should stress that the morphologies in Figs. 2(a)–2(b) are static, i.e., the various fields have settled to fixed-point values. However, the $\mathbf{P}$ field in Figs. 2(c)–2(d) is dynamic.

C. Results for the Coupled System ($c_0 \neq 0$)

Next, let us study the effect of the coupling on the surface-directed dynamics. We have examined all possible combinations of boundary conditions in this context. Here, we only show some representative results.

First, we consider the coupled system with B_P surfaces. Figure 3 presents the snapshots (at $t = 10^4$) of the nematic and active components for $c_0 = 0.1$ (upper row) and 1.0 (lower row). In Figs. 3(a) and 3(d), we show the $\mathcal{S}$-field (see color bar) along with $\mathbf{n}$ (denoted by rods). The corresponding $\mathbf{P}$-field and its magnitude are depicted in Figs. 3(b) and 3(e). Notice the co-alignment of $\mathbf{n}$ and $\mathbf{P}$ due to the coupling. More importantly, the LC morphologies are no longer static

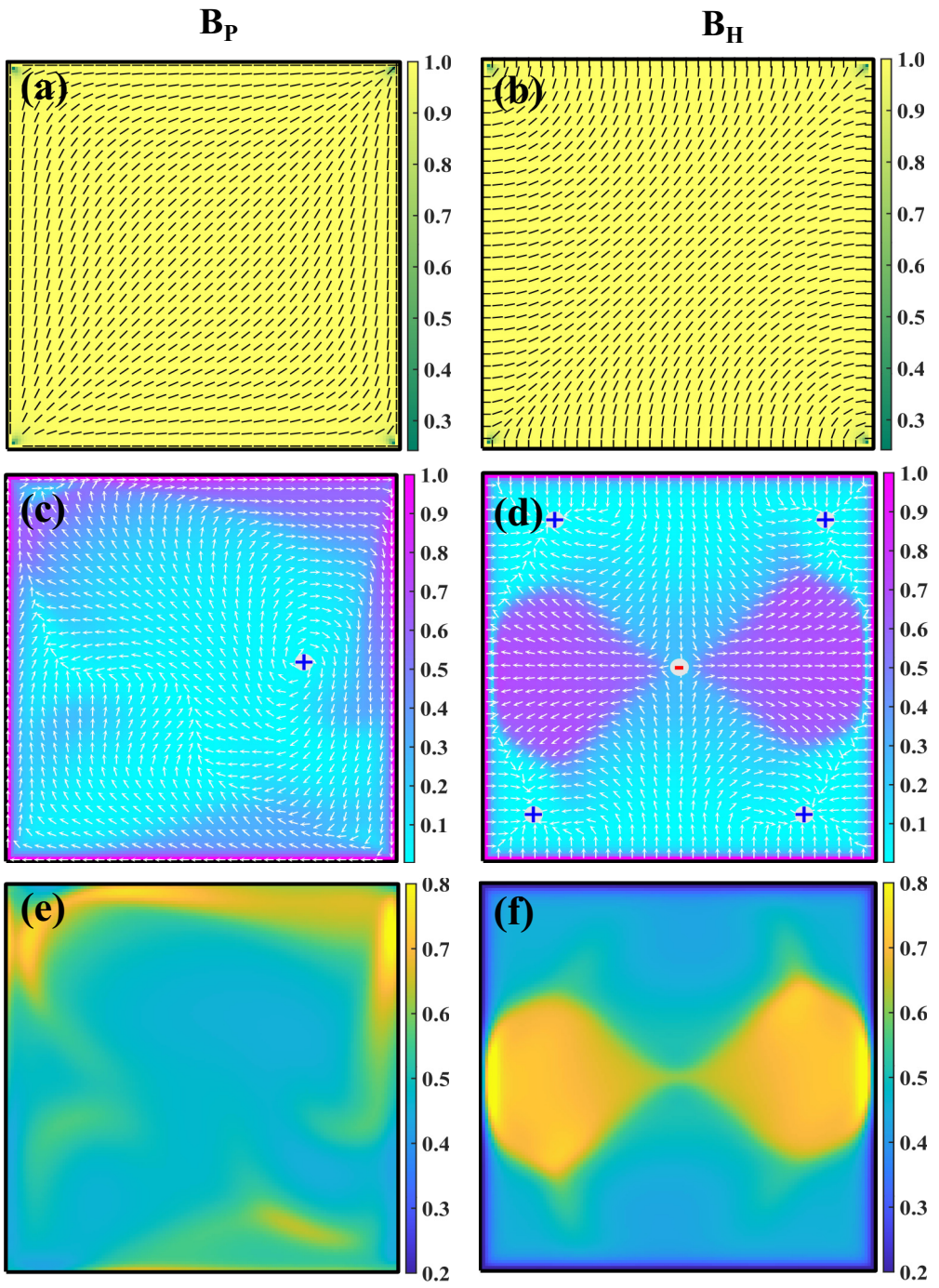

FIG. 2. Snapshots at $t = 10^4$ for the **n**-field (first row), **P**-field (second row), and ρ-field (third row) for $c_0 = 0$. The frames (a), (c), and (e) correspond to planar (B_P) boundary conditions. The color bars in these frames show the nematic orientational order $\mathcal{S}$ in (a); magnitude of polarization $|\mathbf{P}|$ in (c); and density ρ in (e). The rods (arrows) denote the orientation of the director (polarization) field. The defects are denoted by + or –, according to their signs. The corresponding snapshots for homeotropic (B_H) boundaries are shown in frames (b), (d), and (f).

as in Fig. 2(a). Here, the asymptotic LC state consists of two co-rotating topological defects (at a fixed distance d_0) with the same charge $(+1/2)$ at the center of the square well. This dynamic steady state in the passive NLCs is unprecedented and inaccessible in the equilibrium counterpart. These defects move closer with increasing c_0. The corresponding **P**-field exhibits a vortex with $+1$ charge at the center of the square well. The movies of the evolution for both coupling strengths can be found in M2 ($c_0 = 0.1$) and M3 ($c_0 = 1.0$) in the SM [63]. In Figs. 3(c) and 3(f), we show the density field in the system. There is a large variation of ρ in the strongly coupled ($c_0 = 1.0$) system – the dilute regions coincide with the vortex core with $|\mathbf{P}| \simeq 0$. Beyond the anchoring effects at the boundaries, the alignment of nematic molecules is influenced by their interaction with the active fields via the coupling constant c_0. Thus, the observed steady state arises from the interplay between these competing factors. Further, the identical topological charge of both nematic and active components

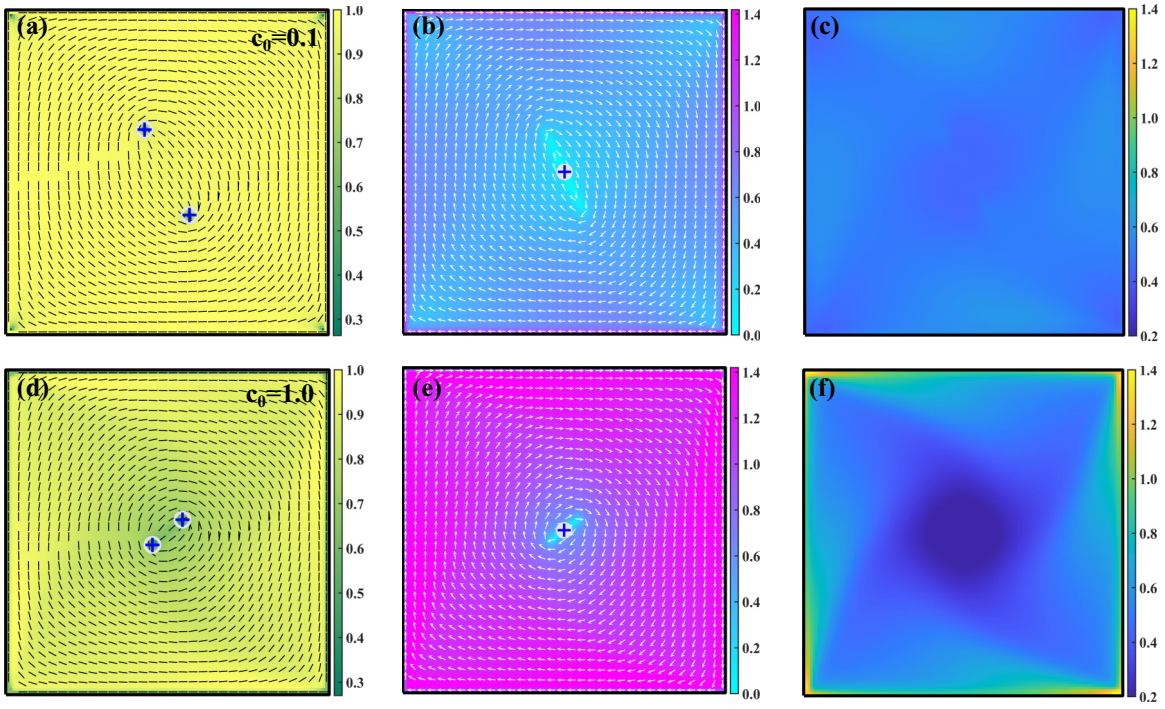

FIG. 3. Snapshots at $t = 10^4$ for the coupled case with $c_0 = 0.1$ (upper row) and $c_0 = 1.0$ (lower row). B_P boundary conditions are imposed at the surfaces for both **n** and **P**. The frames (a) and (d) show the **n**-field; (b), (e) show the **P**-field; and (c), (f) show the ρ-field. The meaning of various symbols and color bars is the same as in Fig. 2.

results in the formation of a structure featuring two $+1/2$ defects. From an application perspective, such morphologies can be harnessed to create a pumping effect in microfluidic devices [6]. The systematic circular motion generates fluid flow inside the devices, which can be channeled in any desired direction.

Before proceeding, we wish to quantify how the morphologies in Fig. 3 change with c_0. The co-rotating vortices in the **n**-field become more tightly bound as c_0 increases. In Fig. 4(a), we plot the intervortex distance d_0 vs. t in the asymptotic state for $c_0 = 0.5, 0.75, 1.0$. The time-series fluctuates chaotically about an average value. In this context, we make two remarks. First, as the spatial mesh size is $\Delta x = 1$, there are inaccuracies in determining the precise locations of the vortex cores. These become more marked at higher c_0 as the vortices come closer together. Second, in the square lattice, there is an intrinsic anisotropy depending on the relative alignment of the line connecting the vortex cores and the diagonal of the square well. We attribute the chaotic fluctuations in $d_0(t)$ vs t to these numerical factors. In Fig. 4(b), we plot the co-rotation angular velocity ω_0 vs t in the asymptotic state for the same values of c_0. In Fig. 4(c), we plot $\bar{d}_0$ vs c_0 on a log-log scale. Here, $\bar{d}_0$ represents the time average of $d_0(t)$ in the asymptotic state. We expect $\bar{d}_0 \to \infty$ as $c_0 \to 0$, corresponding to the uncoupled limit. Our numerical data is consistent with a power-law behavior $\bar{d}_0 \sim c_0^{-\theta}$ with $\theta \simeq 0.60$, though there is a saturation for $c_0 > 1$. In Fig. 4(d), we plot $\bar{\omega}_0$ vs c_0 on a log-log scale. In the uncoupled limit ($c_0 \to 0$), we expect $\bar{\omega}_0 \to 0$. Our numerical data is again consistent with a power-law behavior $\bar{\omega}_0 \sim c_0^{\alpha}$ with $\alpha \simeq 1.25$ for $c_0 < 1$. What consequences do these observations have on AM? We get a flavor from Fig. 3 – the swirling is stronger with increasing c_0, and the AM is pushed closer to the periphery of the well. This is due to the interplay of the inherent linear velocity v_0 and the coupling-induced angular velocity ω_0. These prototypical observations not only demonstrate the symbiotic relationship between LCs and AM, but also provide a systematic procedure for manipulating pattern formation via the coupling strength.

Our second example of coupled kinetics is the case where the LC and AM have B_P and B_H boundary conditions, respectively. The resultant morphologies from our coarsening experiments for $c_0 = 1.0$ are shown in Fig. 5. The snapshots are shown at $t = 10^4$, by which time the dynamics has settled to a fixed point (FP). In Fig. 5(a), we show the $\mathcal{S}$-field with director orientations for the nematogens. No defects are seen in the nematic field. The corresponding **P**-field and its magnitude are shown in Fig. 5(b). The ρ-field is depicted in Fig. 5(c). In the uncoupled limit, the relevant configurations are shown in Figs. 2(a), 2(d), and 2(f). Figure 2(a) shows FP behavior, whereas Figs. 2(d) and 2(f) show complex dynamical states with multiple defects. In Fig. 5, the coupling controls the dynamics of AM and harnesses it to the FP behavior. This state is reminiscent of the experimental observation in [12] where the active particles have higher density in the vicinity of $+1/2$ defects in the nematic field.

IV. SUMMARY AND DISCUSSION

Let us conclude this paper with a summary and discussion of our results. We have focused on the effect of *boundary conditions* (BCs) on the dynamics of *living liquid crystals* (LLCs). They are modeled by the simplest framework that includes a hydrodynamic description for the active flows, but assumes a static LC matrix that acquires a dynamic nematic

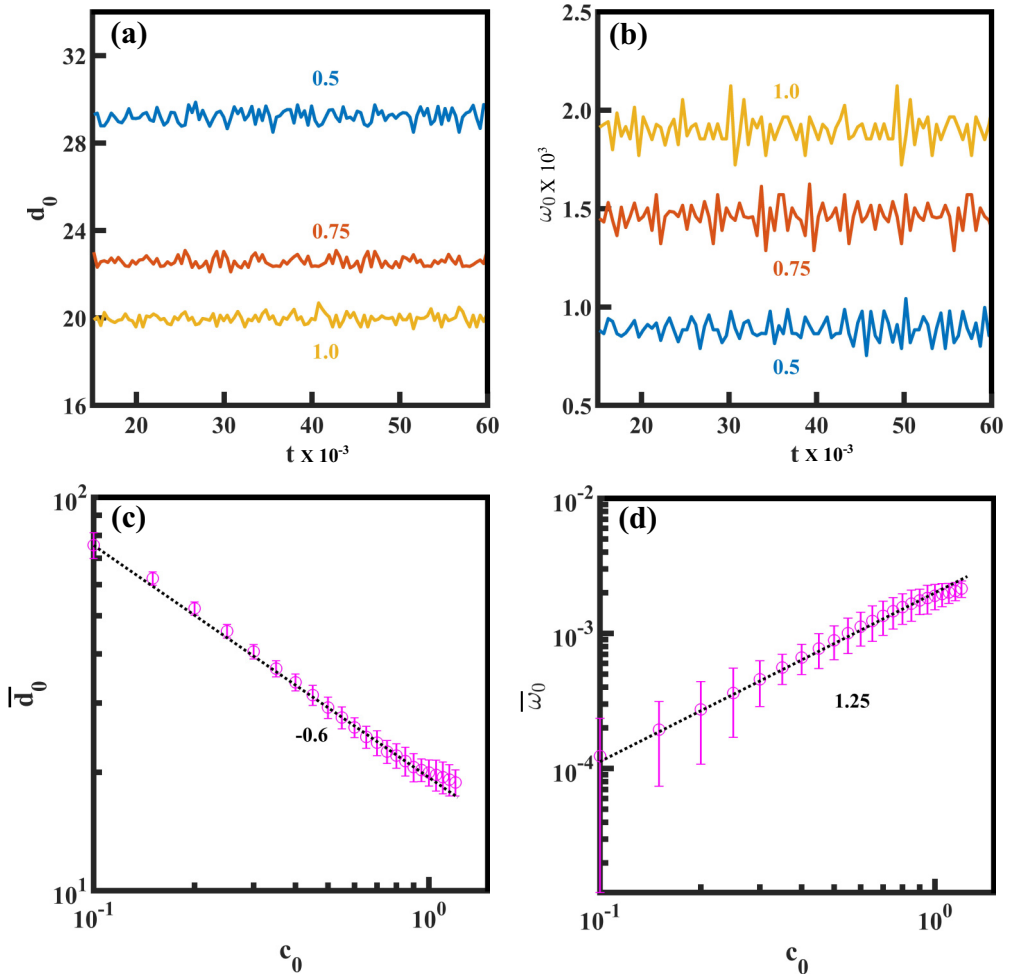

FIG. 4. (a) Plot of the intervortex distance d_0 vs t in the asymptotic state for $c_0 = 0.5,\ 0.75,\ 1.0$. (b) Plot of the co-rotation angular velocity ω_0 vs t for the same c_0-values. (c) Log-log plot of $\bar{d}_0$ vs. c_0. The bar denotes the time-average in the asymptotic state. The dashed line denotes the best linear fit to the data. (d) Log-log plot of $\bar{\omega}_0$ vs c_0.

order via an experimentally motivated coupling term. Our purpose is to examine whether surfaces can be tailored to inject specific dynamical behaviors into an LLC. This control is expected to yield a range of possible applications in science and technology. We consider two types of BC: (a) *planar* or B_P, where **n** or **P** are aligned parallel to the surfaces; and (b) *homeotropic* or B_H, where **n** or **P** point perpendicular to the surface. As $\mathbf{P} \neq -\mathbf{P}$, there are further subclasses in B_P and B_H depending on the direction of **P**. These BCs can arise naturally due to confinement of the LLC in a container. Alternatively, specific BCs may be imposed at surfaces to control the dynamics of the LLC. In this paper, we have shown two representative examples of LLCs in square wells.

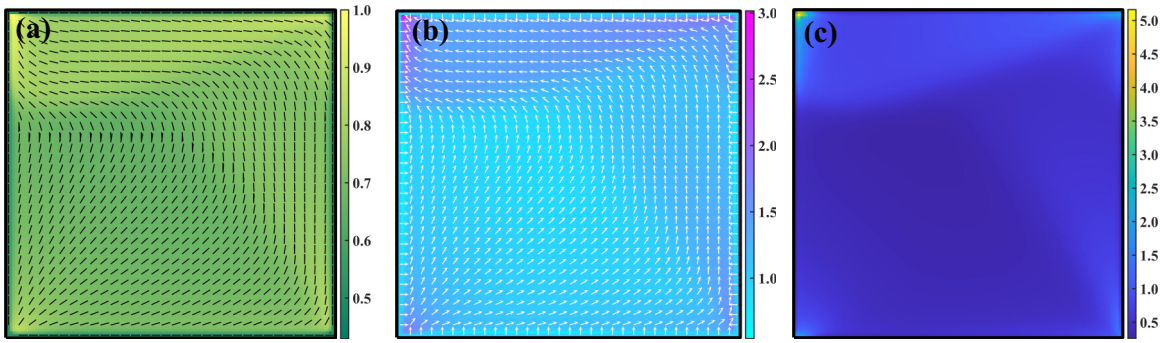

FIG. 5. Snapshots at $t = 10^4$ for the coupled case with $c_0 = 1.0$. The boundary conditions for LCs and AM are B_P and B_H, respectively. The frames show the (a) **n**-field, (b) **P**-field, and (c) ρ-field. The color bars denote the magnitude of the relevant field.

(a) First, we consider the case where **n** has B_P, and **P** has B_P with the directionality being cyclic along the surfaces. In the uncoupled limit, the **n**-field is static, whereas the **P**-field has a single vortex wandering in the system. In the coupled case, the system settles into a controlled dynamics with a co-rotating pair of defects in the **n**-field. The spacing and angular velocity of this co-rotation have a power-law dependence on the coupling strength.

(b) Second, we consider the case where **n** and **P** have B_H, with **P** pointing inward from the surfaces. In the uncoupled limit, the **n**-field is static, and the **P**-field has a complex dynamics with multiple defects, swirling around. In the coupled case, this complex dynamics is tamed and both **n** and **P** settle into a steady state.

We have demonstrated that BCs play a crucial role in pattern dynamics in LLCs. An improved understanding of the interplay between the LLCs and surfaces can help design active systems with specific pattern dynamics. We have studied defect dynamics in LLCs, and investigated the interplay of AM-LC interactions and confining surfaces. In this context, we displayed two important examples from a plethora of dynamical possibilities, e.g., (a) harnessing of random motion into a controlled dynamical trajectory; and (b) taming of a dynamical state to a static state.

The results presented provide only a flavor of surface-directed dynamics in LLCs. There can be several possible extensions of our work. First, the set of parameters in our model is large, primarily because of the large number of parameters in the Toner-Tu equations. We have assigned values to these parameters which are standard for the uncoupled system in the literature. Clearly, a systematic study of parameter space is demanding, but offers intriguing possibilities. Second, it is experimentally more realistic to include spatially anisotropic elastic constants in the LdG free energy for LCs in Eq. (1). This generalization is known to alter the defect dynamics for LCs, and should unfold novel pattern dynamics for LLCs also. Third, an extension of our framework to confined geometries such as discs or channels, or incorporating hydrodynamics in the LC component, should provide unprecedented exotic steady states. Finally, a natural extension of our framework is to $d = 3$. We anticipate rewarding insights, primarily due to the shift from a second-order to a first-order phase transition in the nematic component. The additional dimension is expected to introduce intricate defect structures for both LCs and AM, which should lead to novel coupled dynamics. However, such a study will be challenging as the $3D$ model consists of 9 coupled partial differential equations.

Generally speaking, AM is ubiquitous in nature. The constituent particles tend to parallelize locally, but can exhibit complex unstructured dynamics at the macroscopic level, e.g., turbulent motion. A major research direction in AM has focused on disciplining and harnessing their motion into useful work. Consequently, LLCs are emerging as valuable microfluidic devices with potential applications in sorting and mixing of materials, biosensing, and targeted drug delivery in biomedical applications [31]. We have demonstrated in this work that BCs play a crucial role in pattern dynamics in LLCs. An improved understanding of the interplay between LLCs and surfaces can help design active systems with specific pattern dynamics. We believe that surface-directed behavior opens up the possibility of several novel applications, e.g., active morphologies with persistent motion around a defect core can be used as microfluidic pumps. We hope our present theoretical study will guide future experiments on LLCs, and pave the way for their utilization in devices.

ACKNOWLEDGMENTS

A.V. acknowledges UGC, India for support via a research fellowship. V.B. acknowledges DST, India for research grants. A.V. and V.B. gratefully acknowledge the HPC facility of IIT Delhi for computational resources. We are grateful to the referees for their constructive comments and suggestions. S.P. is grateful to SERB, India for support through a J.C. Bose fellowship.

APPENDIX: DYNAMICAL EQUATIONS FOR LIVING LIQUID CRYSTALS

The dynamical Eqs. (6)–(10) for $d = 2$ living liquid crystals (LLCs) are presented in an expanded form in this Appendix. It is easier to work with the dimensionless form due to the reduced number of parameters, and the identification of universal spatial and temporal scales. For the sake of brevity, we only present the dimensionless forms of Eqs. (6)–(10). These are obtained by introducing rescaled variables as

$$\mathbf{Q} = c_Q\mathbf{Q}', \quad \mathbf{P} = c_P\mathbf{P}', \quad \mathbf{r} = c_r\mathbf{r}', \quad t = c_t t', \quad \text{where}$$
$$c_Q = \sqrt{\frac{|A|}{2C}}; \quad c_P = \sqrt{\frac{\alpha_0}{\beta}}; \quad c_t = \frac{\beta}{\alpha_0\Gamma_Q}\sqrt{\frac{|A|}{2C}}; \quad c_r = \sqrt{\frac{L}{|A|}}. \tag{A1}$$

Dropping the primes, the dimensionless equations can be written as

$$\frac{\partial Q_{11}}{\partial t} = \xi_1\left[\pm Q_{11} - \left(Q_{11}^2 + Q_{12}^2\right)Q_{11} + \nabla^2 Q_{11}\right] + c_0\left(P_1^2 - P_2^2\right), \tag{A2}$$

$$\frac{\partial Q_{12}}{\partial t} = \xi_1\left[\pm Q_{12} - \left(Q_{11}^2 + Q_{12}^2\right)Q_{12} + \nabla^2 Q_{12}\right] + 2c_0 P_1 P_2, \tag{A3}$$

$$\frac{1}{\Gamma}\frac{\partial P_1}{\partial t} = \xi_2\left[\left(\frac{\rho}{\rho_c} - 1 - \mathbf{P}\cdot\mathbf{P}\right)P_1 - \frac{v_1'}{2\rho_0}\nabla_x\rho + \lambda_1'(\mathbf{P}\cdot\nabla)P_1 + \lambda_2'\nabla_x(|\mathbf{P}|^2) + \lambda_3' P_1(\nabla\cdot\mathbf{P}) + \kappa'\nabla^2 P_1\right] + c_0(Q_{11}P_1 + Q_{12}P_2), \tag{A4}$$

$$\frac{1}{\Gamma}\frac{\partial P_2}{\partial t} = \xi_2\left[\left(\frac{\rho}{\rho_c} - 1 - \mathbf{P}\cdot\mathbf{P}\right)P_2 - \frac{v_1'}{2\rho_0}\nabla_y\rho + \lambda_1'(\mathbf{P}\cdot\nabla)P_2 + \lambda_2'\nabla_y(|\mathbf{P}|^2) + \lambda_3' P_2(\nabla\cdot\mathbf{P}) + \kappa'\nabla^2 P_2\right] + c_0(Q_{12}P_1 - Q_{11}P_2), \tag{A5}$$

$$\frac{1}{\Gamma'}\frac{\partial\rho}{\partial t} = -v_0'\nabla\cdot(\mathbf{P}\rho) + D_\rho'\nabla^2\rho. \tag{A6}$$

The ± sign in Eqs. (A2)–(A3) determines whether the nematic component is above (–) or below (+) its critical temperature T_c. For $T < T_c$, the nematic is intrinsically (i.e., for $c_0 = 0$) ordered. For $T > T_c$, the nematic is intrinsically ordered. Similarly, the **P**-field in Eqs. (A4)–(A5) is intrinsically disordered if $\rho_0 < \rho_c$, and intrinsically ordered for $\rho_0 > \rho_c$. The rescaled parameters and their numerical values in our simulations are provided in Table I. These parameter values are similar to those chosen for the uncoupled system (AM or LC) in the literature. However, we emphasize that our simulation results do not change qualitatively on changing the above values as long as the solutions are stable.

TABLE I. Dimensionless parameters in Eqs. (A2)–(A6), and their numerical values.

Scaled Parameters	Numerical Values
$\xi_1 = \frac{2\lvert A\rvert\beta}{\alpha_0}\sqrt{\frac{\lvert A\rvert}{2C}}, \quad \xi_2 = \frac{\alpha_0}{2}\sqrt{\frac{2C}{\lvert A\rvert}}$	1, 1
$v_1' = \frac{v_1}{\alpha_0}\sqrt{\frac{\beta\lvert A\rvert}{\alpha_0 L}}, \quad v_0' = \frac{v_0}{\Gamma_\rho}\sqrt{\frac{\alpha_0\lvert A\rvert}{\beta L}}$	0.5, 0.25
$\Gamma = \frac{\beta\lvert A\rvert\Gamma_P}{\alpha_0\Gamma_Q C}, \quad \Gamma' = \frac{\beta\Gamma_\rho}{\alpha_0\Gamma_Q}\sqrt{\frac{\lvert A\rvert}{2C}}$	1, 1
$\kappa' = \frac{\kappa\lvert A\rvert}{\alpha_0 L}, \quad D_\rho' = \frac{D_\rho\lvert A\rvert}{L}$	1, 1
$\lambda_1' = \frac{\lambda_1}{\Gamma_P}\sqrt{\frac{\lvert A\rvert}{\alpha_0\beta L}}, \quad \lambda_2' = \lambda_2\sqrt{\frac{\lvert A\rvert}{\alpha_0\beta L}}, \quad \lambda_3' = \lambda_3\sqrt{\frac{\lvert A\rvert}{\alpha_0\beta L}}$	−0.5, −0.5, 0.5

[1] S. Ramaswamy, Annu. Rev. Condens. Matter Phys. **1**, 323 (2010).
[2] M. C. Marchetti, J. F. Joanny, S. Ramaswamy, T. B. Liverpool, J. Prost, M. Rao, and R. A. Simha, Rev. Mod. Phys. **85**, 1143 (2013).
[3] L. Angelani, R. Di Leonardo, and G. Ruocco, Phys. Rev. Lett. **102**, 048104 (2009).
[4] A. Sokolov, M. M. Apodaca, B. A. Grzybowski, and I. S. Aranson, Proc. Natl. Acad. Sci. USA **107**, 969 (2010).
[5] R. Di Leonardo, L. Angelani, D. Dell'Arciprete, G. Ruocco, V. Iebba, S. Schippa, M. P. Conte, F. Mecarini, F. De Angelis, and E. Di Fabrizio, Proc. Natl. Acad. Sci. USA **107**, 9541 (2010).
[6] S. P. Thampi, A. Doostmohammadi, T. N. Shendruk, R. Golestanian, and J. M. Yeomans, Sci. Adv. **2**, e1501854 (2016).
[7] A. Kaiser, A. Peshkov, A. Sokolov, B. t. Hagen, H. Löwen, and I. S. Aranson, Phys. Rev. Lett. **112**, 158101 (2014).
[8] A. J. T. M. Mathijssen, F. Guzmán-Lastra, A. Kaiser, and H. Löwen, Phys. Rev. Lett. **121**, 248101 (2018).
[9] A. Sokolov, S. Zhou, O. D. Lavrentovich, and I. S. Aranson, Phys. Rev. E **91**, 013009 (2015).
[10] S. Zhou, A. Sokolov, O. D. Lavrentovich, and I. S. Aranson, Proc. Natl. Acad. Sci. USA **111**, 1265 (2014).
[11] C. Peng, T. Turiv, Y. Guo, Q.-H. Wei, and O. D. Lavrentovich, Science **354**, 882 (2016).
[12] M. M. Genkin, A. Sokolov, O. D. Lavrentovich, and I. S. Aranson, Phys. Rev. X **7**, 011029 (2017).
[13] I. S. Aranson, Acc. Chem. Res. **51**, 3023 (2018).
[14] A. Sokolov, A. Mozaffari, R. Zhang, J. J. De Pablo, and A. Snezhko, Phys. Rev. X **9**, 031014 (2019).
[15] O. D. Lavrentovich, Curr. Opin. Colloid Interface Sci. **21**, 97 (2016).
[16] M. J. Stephen and J. P. Straley, Rev. Mod. Phys. **46**, 617 (1974).
[17] J. Prost and P. G. de Gennes, *The Physics of Liquid Crystals* (Oxford University Press, Oxford, UK, 1995), Vol. 83.
[18] A. Doostmohammadi, J. Ignés-Mullol, J. M. Yeomans, and F. Sagués, Nat. Commun. **9**, 3246 (2018).
[19] S. Zhou, Liquid Crystals Today **27**, 91 (2018).
[20] P. C. Mushenheim, R. R. Trivedi, H. H. Tuson, D. B. Weibel, and N. L. Abbott, Soft Matter **10**, 88 (2014).
[21] C. Lapointe, A. Hultgren, D. Silevitch, E. Felton, D. Reich, and R. Leheny, Science **303**, 652 (2004).
[22] I. Musevic, M. Skarabot, U. Tkalec, M. Ravnik, and S. Zumer, Science **313**, 954 (2006).
[23] M. Ravnik and J. M. Yeomans, Phys. Rev. Lett. **110**, 026001 (2013).
[24] H. H. Wensink and H. Löwen, Phys. Rev. E **78**, 031409 (2008).
[25] H. Wioland, F. G. Woodhouse, J. Dunkel, J. O. Kessler, and R. E. Goldstein, Phys. Rev. Lett. **110**, 268102 (2013).
[26] E. Lushi, H. Wioland, and R. E. Goldstein, Proc. Natl. Acad. Sci. USA **111**, 9733 (2014).
[27] S. Zhou, O. Tovkach, D. Golovaty, A. Sokolov, I. S. Aranson, and O. D. Lavrentovich, New J. Phys. **19**, 055006 (2017).
[28] S. M. Fielding, D. Marenduzzo, and M. E. Cates, Phys. Rev. E **83**, 041910 (2011).
[29] Y. Fily, A. Baskaran, and M. F. Hagan, Soft Matter **10**, 5609 (2014).
[30] M. Theillard, R. A. Matilla, and D. Saintillan, Soft Matter **13**, 363 (2017).
[31] R. Zhang, A. Mozaffari, and J. J. de Pablo, Nat. Rev. Mater. **6**, 437 (2021).
[32] S. E. Spagnolie and P. T. Underhill, Annu. Rev. Condens. Matter Phys. **14**, 381 (2023).
[33] J. P. Hernandez-Ortiz, C. G. Stoltz, and M. D. Graham, Phys. Rev. Lett. **95**, 204501 (2005).
[34] A. Kudrolli, G. Lumay, D. Volfson, and L. S. Tsimring, Phys. Rev. Lett. **100**, 058001 (2008).
[35] X. Yang, M. L. Manning, and M. C. Marchetti, Soft Matter **10**, 6477 (2014).
[36] J. Deseigne, S. Léonard, O. Dauchot, and H. Chaté, Soft Matter **8**, 5629 (2012).
[37] G. Wells and C. Brown, Appl. Phys. Lett. **91**, 223506 (2007).
[38] R. Barberi, J. Bonvent, M. Giocondo, M. Iovane, and A. Alexe-Ionescu, J. App. Phys. **84**, 1321 (1998).
[39] C. Tsakonas, A. Davidson, C. Brown, and N. J. Mottram, Appl. Phys. Lett. **90**, 111913 (2007).
[40] H. Kusumaatmaja and A. Majumdar, Soft Matter **11**, 4809 (2015).
[41] C. Luo, A. Majumdar, and R. Erban, Phys. Rev. E **85**, 061702 (2012).
[42] A. Majumdar and A. Lewis, Liq. Cryst. **43**, 2332 (2016).

[43] M. Robinson, C. Luo, P. E. Farrell, R. Erban, and A. Majumdar, Liq. Cryst. **44**, 2267 (2017).
[44] G. Barbero and L. R. Evangelista, *Adsorption Phenomena and Anchoring Energy in Nematic Liquid Crystals* (CRC Press, Boca Raton, Florida, 2005).
[45] K. Bisht, V. Banerjee, P. Milewski, and A. Majumdar, Phys. Rev. E **100**, 012703 (2019).
[46] K. Bisht, Y. Wang, V. Banerjee, and A. Majumdar, Phys. Rev. E **101**, 022706 (2020).
[47] A. Vats, P. K. Yadav, V. Banerjee, and S. Puri, Phys. Rev. E **108**, 024701 (2023).
[48] J. Toner and Y. Tu, Phys. Rev. Lett. **75**, 4326 (1995).
[49] J. Toner and Y. Tu, Phys. Rev. E **58**, 4828 (1998).
[50] A. J. Bray, Adv. Phys. **51**, 481 (2002).
[51] E. Priestly, *Introduction to Liquid Crystals* (Springer Science & Business Media, Berlin, 2012).
[52] A. Vats, V. Banerjee, and S. Puri, Europhys. Lett. **128**, 66001 (2020).
[53] A. Vats, V. Banerjee, and S. Puri, Soft Matter **17**, 2659 (2021).
[54] A. Vats, S. Puri, and V. Banerjee, Phys. Rev. E **106**, 044701 (2022).
[55] E. Bertin, M. Droz, and G. Grégoire, J. Phys. A: Math. Theor. **42**, 445001 (2009).
[56] S. Puri, in *Kinetics of Phase Transitions* (CRC Press, Boca Raton, Florida, 2009), pp. 13–74.
[57] G. P. Alexander, B. G.-g. Chen, E. A. Matsumoto, and R. D. Kamien, Rev. Mod. Phys. **84**, 497 (2012).
[58] C. Bechinger, R. Di Leonardo, H. Löwen, C. Reichhardt, G. Volpe, and G. Volpe, Rev. Mod. Phys. **88**, 045006 (2016).
[59] D. Kincaid and E. W. Cheney, *Numerical Analysis: Mathematics of Scientific Computing* (American Mathematical Soc., Providence, RI, 2009), Vol. 2.
[60] J. Walton, N. J. Mottram, and G. McKay, Phys. Rev. E **97**, 022702 (2018).
[61] R. Green, J. Toner, and V. Vitelli, Phys. Rev. Fluids **2**, 104201 (2017).
[62] K. T. Wu, J. B. Hishamunda, D. T. Chen, S. J. De Camp, Y.-W. Chang, A. Fernández-Nieves, S. Fraden, and Z. Dogic, Science **355**, eaal1979 (2017).
[63] See Supplemental Material at http://link.aps.org/supplemental/10.1103/PhysRevE.110.034701 for movies depicting pattern dynamics in our coarse-grained model.